International Journal of Rock Mechanics and Mining Sciences 105 (2018) 98–109

Contents lists available at ScienceDirect

International Journal of Rock Mechanics and Mining Sciences

journal homepage: www.elsevier.com/locate/ijrmms

# A progressive S-shaped yield criterion and its application to rock pillar behavior

Sankhaneel Sinha*, Gabriel Walton

*Colorado School of Mines, Golden, CO, USA*

ARTICLE INFO

*Keywords:*
Rock pillar
Yield criterion
Numerical modelling

ABSTRACT

Yielding of hard rock pillars under moderate to high stresses involves the formation of excavation-parallel extensile fractures. In recent decades, researchers have found that this behavior can be best replicated by a Cohesion-Weakening-Frictional-Strengthening (CWFS) model which captures the non-simultaneous mobilization of cohesion and friction; this is a mechanism that has been experimentally proved to occur in rocks undergoing brittle failure. In the context of rock pillars, the extensile fracturing process is limited only to the surficial portions. The inner core of rock pillars, on the other hand, fails through a shear mechanism. A realistic rock strength criterion must therefore account for the two different failure behaviors. To this end, this study introduces an improved yield criterion that represents small-scale damage processes (extensile cracking under low confinement and semi-brittle shear under higher confinement) while exhibiting an emergent pillar behavior consistent with what has been observed in the field. The failure criterion was implemented in the finite difference software FLAC$^{3D}$ which was then used to investigate the effect of width to height and length to width ratios on the strength of pillars.

## 1. Introduction

With advances in technology and gradual depletion of near-surface ores, it becomes essential to exploit increasingly deeper deposits. Present day metal and non-metal mines have descended to depths beyond 2 km, where the magnitudes of pre-mining stresses are very high. In such highly stressed ground, most mining systems rely primarily on unmined rock pillars for maintaining the functional integrity of underground openings and roadways. Generally speaking, a pillar is capable of supporting the overburden load as long as its strength exceeds the applied stress. Two-dimensional and three-dimensional numerical models are often used to evaluate the stability of mine structures, including pillars.

There are three broad classifications of numerical modelling methods: continuum, discontinuum and hybrid. Each method has its own advantages and disadvantages in context of ground control problems. The continuum method treats the ground as an equivalent continuous material with properties that approximately reflect the effect of joints and discontinuities.[1] Although this method lacks the ability to explicitly capture stress-induced fracturing, it has been successfully used to model case studies under various geological and mining conditions.[2–11] For relatively competent rockmasses which deform primarily through stress-induced damage to intact rock, continuum modelling represents a useful analysis approach.

The accuracy of continuum model results is heavily governed by the selection of a proper yield criterion and associated input parameters. Selection of a yield criterion for a particular set of conditions is ideally based on knowledge of the micro-mechanical damage processes that ultimately control the global failure of the system. In this study, a new yield criterion for intact rock is proposed, and its ability to produce model results consistent with pillar behaviors observed in-situ is demonstrated. Previous modelling attempts using Hoek-Brown,[12] strain-softening Mohr-Coulomb[13,14] and S-shaped yield criterion[15] have predicted a near-exponential increase in strength with W/H ratio which contradicts the convex shape of empirical pillar strength equations[16,17] as well as the trend obtained in this study. The differences in observed behavior is likely related to the inability of the three criteria to appropriately capture the damage mechanisms of intact rocks.

In-situ damage processes in crystalline rocks were first systematically analyzed at Canada's Underground Research Laboratory (URL) and Sweden's Aspo URL. These studies documented the development of brittle spalling and fracture generation in massive granitic rocks and provided a better understanding of brittle rockmass behavior.[18,19] It was found that in massive to sparsely fractured rock under high stress conditions, damage near excavation boundary was dominated by extensile fractures, which macroscopically appeared as spalling.[20–23] The

* Corresponding author.
*E-mail address:* sankhaneelsinha@mymail.mines.edu (S. Sinha).

https://doi.org/10.1016/j.ijrmms.2018.03.014
Received 11 August 2017; Received in revised form 11 December 2017; Accepted 18 March 2018
Available online 13 April 2018
1365-1609/ 

surface-parallel fracturing process was primarily a cohesion-loss process, followed by mobilization of friction.[24,25] Attempts to numerically simulate this behavior using shear yield models were not met with success.[2,18,26] This is not surprising, since the yield criterions were based on laboratory tests where the mode of failure was primarily shear.[18,27] A failure criterion is not expected to reproduce multiple failure modes unless the underlying physical mechanisms are similar.[28]

The inability of shear yield criteria to model the brittle failure behavior sparked the development of a Cohesion-Weakening-Frictional-Strengthening (CWFS) model.[2] The CWFS model is a strain-dependent yield criterion which accounts for the non-simultaneous mobilization of friction and cohesion. The changes in these two strength components is controlled by plastic shear strain - a variable which is used as a proxy for damage.[2,9,23] Since its development, the CWFS model has been successfully used in replicating the stress-induced notch formations around the periphery of tunnels.[2,4,5] However, most of the previous studies only focused on rockmass behavior under low confinement conditions. This study considers the behavior of rocks under low as well as high confinement, by using pillars as the study context due to their potential to experience wide ranges of confinements across their extents.

The applicability of the CWFS model should be restricted to the low-confinement surficial portions of a pillar because as the rock at the excavation boundary dilates, it increases the confining stresses within the pillar which in turn suppresses the formation of extensile cracks. This has been mathematically demonstrated using the concepts of fracture mechanics.[21] It therefore follows that a CWFS model alone is not sufficient in describing the failure behavior of a rock pillar over the entire range of confinement likely to be experienced by the rockmass. A comprehensive yield criterion must reflect the brittle failure mechanism at low confinement and shear failure mechanism at higher confinement.

The authors suggest the need to use a progressive S-shaped strength envelope that can account for the different failure mechanisms in the different confinement regimes. In the last decade, an S-shaped failure envelope was conceived by Diederichs[23] and formalized by Kaiser et al.[15] This envelope has a strong theoretical basis and combines the CWFS strength model at low confinement and a conventional shear yield envelope at higher confinement. Nevertheless, these precursory studies only describe the final shape of the envelope, ignoring the evolutionary nature of the damage process. As will be shown later in this study, it is not sufficient to capture the shape of only the ultimate strength envelope; the complete strength envelope must be defined for all material states (i.e. with respect to material damage). The reason is the complex interrelationships between the mobilization of cohesion, friction, and dilation that ultimately control material behavior. Without accounting for the evolution of these parameters, small-scale damage and stress re-distribution processes are not captured properly. In summary, a rock yield criterion must satisfy two important criteria: (a) account for the evolving nature of the damage process, and, (b) be consistent with the expected damage mechanisms for the entire range of expected confining stresses.

The progressive S-shaped yield criterion as proposed in this study satisfies both these criteria and when incorporated in the finite difference software, FLAC$^{3D}$, it can be used to replicate some well-documented pillar behaviors seen in the field. This study utilizes the calibrated rockmass parameters of Walton et al.[9] and Walton and Diederichs[10] as a starting point for the pillar models. The choice of the two case studies was based on their disparate rock UCS value - the Creighton granite[9] has a UCS of 220 MPa while the studied conglomerate has a lower UCS of 95 MPa.[10] The pillar model was used to investigate the effect of $W/H$ and $L/W$ ratios on the global strengths of pillars. The focus of this study is to introduce the progressive S-shaped criterion and demonstrate its capabilities in reproducing observed pillar behaviors.

## 2. Development of a progressive S-shaped yield criterion

The progressive S-shaped yield criterion satisfies the two important and fundamental criteria of a realistic rock yield criterion. This section will elucidate how the two criteria are met and provide mechanistic interpretation regarding the different segments of the envelope. The development of the criterion was motivated by the need for an improved failure envelope for numerical modelling as evidenced by the inability of previous continuum modelling attempts to replicate observed rock pillar strength trends. Some recommendations for selection of material parameters for the criterion will also be provided.

The evolving nature of the damage process was captured by relating the different segments of the envelope to the incremental plastic parameter, mathematically defined by[29]:

$$\Delta\epsilon^{ps} = \frac{1}{\sqrt{2}}\sqrt{(\Delta\epsilon_1^p - \Delta\epsilon_m^p)^2 + (\Delta\epsilon_m^p)^2 + (\Delta\epsilon_3^p - \Delta\epsilon_m^p)^2} \quad (1)$$

$$\Delta\epsilon_m^p = \frac{1}{2}(\Delta\epsilon_1^p + \Delta\epsilon_3^p) \quad (2)$$

where $\Delta\epsilon^{ps}$is the incremental plastic parameter, $\Delta\epsilon_1^p$ and $\Delta\epsilon_3^p$ are the plastic strain increments in the principal directions. There is no globally accepted indicator that can quantify system damage corresponding to a particular stress/strain level. As a solution, Itasca[29] developed the incremental plastic parameter and has been using it in FLAC and FLAC$^{3D}$. This parameter has two major advantages: (a) Easy implementation in constant-strain quadrilateral (in FLAC$^{3D}$) and triangular (in FLAC$^{2D}$) zones, and, (b) Approximate linear relationship with maximum plastic shear strain ($\gamma_p$) given by $\epsilon^{ps} = \frac{1}{2}\gamma^p$.[30] The plastic shear strain corresponding to the degradation of cohesion and mobilization of friction for different rock types can be estimated from loading-unloading tests on laboratory scale samples.

The progressive S-shaped criterion has three basic envelopes: (a) Yield, (b) Peak, and, (c) Residual (Fig. 1). Each of these envelopes corresponds to a particular cumulative plastic shear strain ($\epsilon^{ps} = \sum \Delta\epsilon^{ps}$); these values depend heavily on the rock being considered. The evolution of the yield into peak and residual envelope ensures that the evolving nature of the damage process is accounted for.

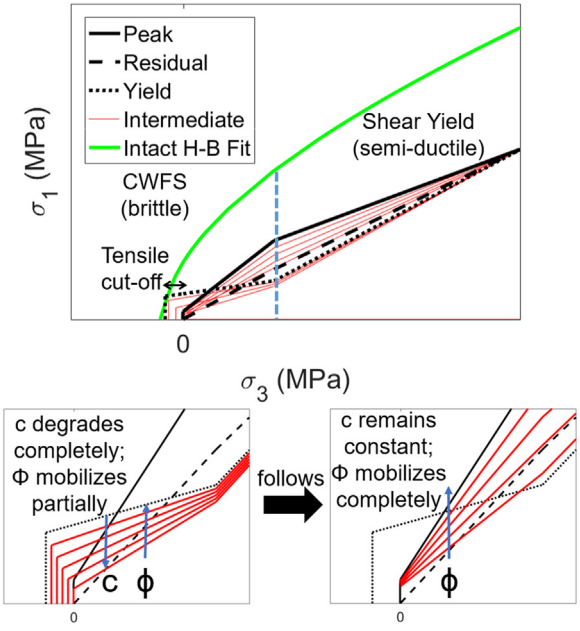


**Fig. 1.** Conceptual model of the progressive S-shaped yield criterion in principal stress space along with the intact rock Hoek-Brown (H-B) envelope. The red lines depict intermediate strength envelopes. (For interpretation of the references to color in this figure legend, the reader is referred to the web version of this article.)

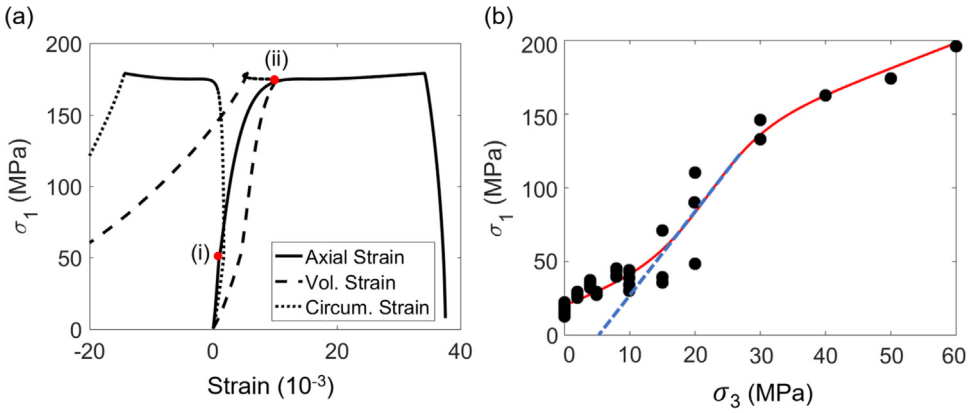


**Fig. 2.** (a) Axial, volumetric and circumferential strain versus minimum principal stress for an Indiana Limestone sample at $\sigma_3 = 50$ MPa, (b) Modified Boltzmann sigmoid curve fitted to 54 crack volumetric strain reversal datapoints (20 uniaxial and 34 triaxial).

The left and the right portion of the criterion, separated by a blue line in Fig. 1, exhibit the characteristics of a CWFS and shear yield model, respectively. The bimodal nature of the envelope allows the criterion to represent both distinctive failure mechanisms.

The plastic shear strain corresponding to the degradation of cohesion ($\epsilon_c^{ps}$) and mobilization of friction ($\epsilon_\emptyset^{ps}$) may or may not be equal for a particular rock. For example, the Creighton granite has $\epsilon_c^{ps} = 0.0025$ and $\epsilon_\emptyset^{ps} = 0.0055$[9] while the studied Conglomerate has $\epsilon_c^{ps} = \epsilon_\emptyset^{ps} = 0.003$.[10] The change from one intermediate envelope to the next, as a function of the plastic shear strain, must account for the similar/dissimilar $\epsilon_c^{ps}$, $\epsilon_\emptyset^{ps}$ values. To illustrate how this can be achieved within the framework of the progressive S-shaped criterion, consider Fig. 1 corresponding to Creighton granite. In this case, the cohesion degrades completely with partial friction mobilization ($\epsilon^{ps} = 0 - 0.0025$), followed by constant cohesion (at its degraded level) and complete mobilization of friction ($\epsilon^{ps} = 0.0025 - 0.0055$). In such a case, a fourth envelope has to be defined between the peak and yield envelope which corresponds to the degraded cohesion and semi-mobilized friction angle. The semi-mobilized friction angle can be computed by proportionally scaling it with plastic shear strain. In cases where $\epsilon_c^{ps} = \epsilon_\emptyset^{ps}$, friction mobilizes and cohesion degrades simultaneously, eliminating the need for an intermediate envelope.

The diverging trend of the intact Hoek-Brown fit and Crack Damage (CD) threshold (right side of the peak envelope) in Fig. 1 is consistent with the findings of Martin.[18] Even though the rock analyzed by Martin[18] is not mineralogically same as Creighton granite, the authors expect them to behave in a similar fashion, given their granitic composition, comparable strength and damage threshold levels. The CD threshold in Fig. 1 was found to be 76% of the HB fit at $\sigma_3 = 0$, which is slightly higher than that obtained by Martin.[18] This discrepancy could be attributed to the choice of a linear CD representation in the progressive S-shaped criterion over the curved representation adopted by Martin.[18]

The progressive S-shaped criterion has fourteen input parameters in total: 6 cohesions, 6 friction angles and 2 plastic shear strains to constrain the evolution of the yield surface. When developing this criterion, two assumptions were made: (a) the intersection point of the low and high confinement portion will be constant for all envelopes, and, (b) all envelopes will coincide for some value of confinement (the point at which deformation becomes perfectly plastic). These two constraints reduce the degrees of freedom such that the entire criterion can be defined by eleven principal parameters instead of fourteen.

The methodology recommended for generating a progressive S-shaped criterion for a given rock type is as follows: (a) First, the cohesion, friction angle and plastic shear strain for peak envelope is selected. (b) The confining stress which separates the high and low confinement portions is then computed. (c) Next, the cohesion of the left side and the friction angle for both sides of the Yield envelope is selected. The cohesion for the right side of the Yield envelope could then be calculated to ensure the same intersection point of the low and high confinement portions of the Yield envelope as for the Peak envelope. This then constrains the confining stress point at which all three envelopes would coincide. (e) Finally, the cohesion and friction angle of the left side of the residual envelope is selected. The right segment of the residual envelope is calculated based on the two constraints stated above.

### 2.1. Yield envelope

The left portion of the yield envelope corresponds to the Crack Initiation (CI) threshold while the right portion follows a modified form of the Mogi's Line. CI marks the onset of random extensile cracking, with cracks mostly oriented along the direction of maximum principal stress ($\sigma_1$). For brittle cracking (eg. CWFS model), CI has been found to be an appropriate representation of the initial in-situ yield threshold[9,18,23] and can be determined using acoustic emission techniques,[31] volumetric stress-strain curve[32] and/or axial/lateral stress-strain curves.[23,33,34]

In the initial phases of formulation, CI was considered as the first point of yield over the entire range of confinement, including for shear yield. It is unclear, however, what the general mechanistic significance of CI is for failure mechanisms which are not brittle in nature. Some recent laboratory tests on Indiana Limestone indicated that at higher confinement, when the failure mechanism transitions from brittle to semi-ductile, the initial yield is governed by a steeply inclined line (relative to CI) with a slope similar to that of Mogi's line.[35] The reason for such a behavior is intuitive; the increased confinement suppresses the formation of tensile cracks causing the initial strength to extend above CI. From the axial stress-strain, axial stress-volumetric strain and axial stress-circumferential strain plot of an Indiana Limestone sample tested at 50 MPa confinement (Fig. 2a), it can be seen that although some axial strain non-linearity initiates at Point i, the volumetric strain reversal does not occur until the stress level is close to peak (Point ii). The high lateral confinement suppresses the lateral dilation forcing grain-scale rearrangement to occur between points i and ii.

For the same set of laboratory tests on Indiana Limestone, a modified Boltzmann sigmoid curve has been fit to fifty-four crack volumetric strain reversal datapoints (Fig. 2b). The zone of transition, marked by a blue dotted line, has a negative intercept and a slope of about 5.5 which is significantly steeper than the Mogi's line.[36] Such a gradient is not surprising, given the fact that the Mogi's line is an overall fit to a curved envelope[37] over a confinement range of 0–600 MPa; the actual slope of the brittle-ductile transition line, even for non-carbonate rocks, can be significantly different at lower

confinement levels. For a low porosity rock like Creighton granite (< 1%), where the grains have limited ability for rearrangement, the slope of the brittle ductile transition should be closer to 4.4. Over the course of model calibration, this was ultimately chosen to be 3.8 for this study.

The point of crack volumetric strain reversal is generally used as the in-situ yield strength even though it does not coincide with the point of axial strain non-linearity. For instance, in CWFS strength model, CI is used as the in-situ yield although yield initiates at CD in laboratory. Under high confinement, however, axial strain non-linearity begins at an early stage (Point i; Fig. 2a). The lateral strain curve remains linear up to total volumetric strain reversal (Point ii; Fig. 2a) or crack volumetric strain reversal, both of which coincide beyond the brittle-ductile transition.[35] In light of the previous discussion and to ensure consistency with the in-situ definition of crack volumetric strain reversal, the modified Mogi's Line has been chosen as the right side of the Yield Envelope. To define the slope of the right portion of the yield envelope, the authors suggest conducting laboratory triaxial testing where possible. If it is not feasible to achieve the required confinement level, this parameter could be obtained from back analysis instead.

### 2.2. Peak envelope

The left portion of the peak envelope is coincident with the Spalling Limit while the right portion is defined by the Crack Damage (CD) threshold. The spalling limit describes the ultimate strength of spalled ground at low confinement (more specifically, it is the residual strength at very low confinement and mobilized strength at moderate confinement). In the principal stress space, it can be mathematically represented by $\sigma_1/\sigma_3 = 10–20$, corresponding to a friction angle of 55–65°.[23,38] This relationship assumes zero residual cohesion; in reality, this may be non-zero depending on the structure and petrographic characteristics of the rock. Recently, Walton[39] conducted a statistical study on back-analyzed CWFS input parameters available in literature. This study provides guidelines on selection of peak cohesion, peak friction and residual friction. In absence of any laboratory data, these could be used as a starting point for numerical models.

The slope of the spalling limit, referred to here as the mobilized friction angle, is related to the peak frictional component of strength and can be correlated with the $m_i$ parameter of Hoek-Brown failure criterion. To estimate the slope of the spalling limit, the authors suggest determining $m_i$ from tensile strength, uniaxial and triaxial strength data and then employing the relationship proposed by Walton.[39] An empirical estimate of $m_i$ can also be obtained from tables such as those published by Marinos and Hoek.[40]

The Crack Damage threshold (CD) marks the onset of unstable crack interaction and is oftentimes referred to as long-term laboratory shear strength.[24] Prior to achieving CD, tensile microcracks remain randomly distributed throughout a sample. When a critical crack intensity is attained, these microcracks interact forming meso-cracks.[21] Further interaction and propagation of these cracks lead to the formation of a shear failure plane.

Previous experimental observations have confirmed the peak strength to be a system-dependent variable (specifically, a function of specimen geometry and loading conditions).[41] Martin and Chandler[24] identified the CD to be a true material property. Based on the fact that pillar loading is a slow phenomenon, CD threshold was chosen as the peak shear strength envelope instead of the short-term laboratory peak envelope. CD is generally associated with inelastic deformation in the axial direction ($\sigma_1$) and can be determined as the point of non-linearity in the axial stress-strain curve or the point of reversal in the axial strain-volumetric strain curve obtained from laboratory compression testing.[42] It can also be identified using acoustic emission techniques.[31,42,43]

### 2.3. Residual envelope

The residual envelope was derived through simultaneous degradation of both portions of the peak envelope. The reduction in the right portion of the envelope is analogous to the degradation from peak to residual in a conventional shear strength model. The rationale behind degrading the left portion is based on the experimental observations of Martin and Chandler[24] who found that with increasing damage, friction reduces by 30–50% while cohesion remains constant. Again, due to absence of sufficient laboratory data, no general guideline for selecting this portion of the envelope could be established. Ultimately, it will be demonstrated later in this paper that the strength of pillars is not significantly affected by the residual envelope. This is because of the large plastic strain lag between the peak and the residual envelope used in the model. Based on the findings of Martin and Chandler,[24] a 30–50% reduction in friction angle of spalling limit over 4 times the plastic shear strain associated with the peak envelope was employed in this study.

## 3. Application of the progressive S-shaped yield criterion in modelling pillars

The primary objective of this paper is to establish an improved rock yield criterion that can be easily implemented in modelling software. For the purposes of this study, the progressive S-shaped criterion was implemented in FLAC$^{3D}$.[29] FLAC$^{3D}$ is a three-dimensional finite difference code developed by Itasca that is used by researchers and consultancy firms worldwide. The bilinear strain-softening ubiquitous joint plastic constitutive model was selected for this study. This model was selected as it allowed for two yield surface segments to be used, as is required for the progressive S-shaped criterion, and it also allowed for each segment to evolve as a function of cumulative plastic shear strain.

The focus of this study is on those geologic conditions where the behavior of the system of interest (in this case, a pillar) is governed by damage to intact material rather than by deformation along distinct structural features. Since the effect of through-going joints or pre-defined planes of weakness is not relevant here, very high strength properties were assigned to the ubiquitous joints. Previous studies have found CI and CD threshold limits to be true material properties for intact rocks.[24,42] Since fractures were not considered in the current study, a laboratory to field scale degradation in parameters was not applicable.

### 3.1. Model development

An 8 m cubic pillar model with 0.166 m mesh elements was developed and loaded quasistically through two elastic beams on either side (Fig. 3). Roller boundaries were assigned to the sides of the beam while the top and the bottom surfaces were subjected to a constant velocity boundary condition. To eliminate the dynamic effects of loading, a very low velocity ($5 \times 10^{-8}$ m/step) was selected. This was based on a sensitivity analysis of the effect of loading rate on the pre- and post-peak portion of the stress-strain curve. The pillar corners were rounded with two rows of elements to ensure a smooth transfer of stress through the model. Other variations of rounding (i.e. non-rounded, 1, 2, 3 and 4 rows of elements) were tested as a part of model development. It was found that beyond 2-element rounding, the stress and displacement contours were relatively consistent. Additionally, the 2-element rounding geometry represents a reasonable approximation of the typical shape of pillars in the field.

The rock mass parameters of Creighton granite[9] were used as a starting point for the pillar models which were tested. During the calibration process, they were adjusted to reproduce the empirical pillar strength curve, which will be discussed in Section 4.1. The Creighton mine case study was performed using the classical CWFS strength model; therefore, only some of the relevant parameters, like the cohesion and friction for the left portions of the Yield and Peak Envelope,

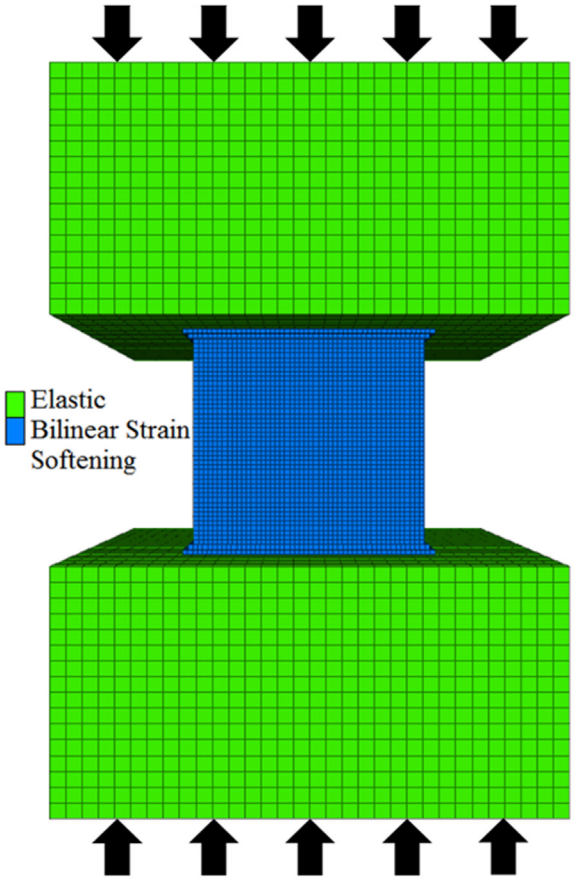


**Fig. 3.** Pillar model geometry used in this study.

were available. The outstanding parameters had to be estimated from uniaxial and triaxial datasets for similar rock type. Table 1 lists the calibrated parameters of the progressive S-shaped criterion in $\sigma_1$-$\sigma_3$ space and the plastic shear strains associated with them. The rockmass input parameters for the bilinear strain softening model was computed using Eqs. (3) and (4) and are also listed in Table 1.

$$c = \frac{UCS \quad (1-\sin\varphi)}{2cos\varphi} \tag{3}$$

$$\varphi = sin^{-1}(\frac{k-1}{k+1}) \tag{4}$$

where $c$ is cohesion, $\varphi$ is friction angle, and $k$ is the slope of the envelope in $\sigma_1 - \sigma_3$ space.

Mechanistically speaking, the plastic shear strain corresponding to the degradation of cohesion and mobilization of friction is an inherent property of a particular rock. However, since the formulation of FLAC$^{3D}$ requires partitioning the problem domain into constant-strain quadrilaterals, the dimension of the yield region is dictated by the zone edge length. As such, the plastic shear strain selected for different mesh sizes will generate different model results (in terms of the volume of failed rock mass and associated stress redistribution process). This has a serious implication on the applicability of laboratory derived plastic strain values to numerical models. A viable solution, recommended by Itasca, is to recalibrate the model to field measurements every time the mesh dimension is modified.[44] Itasca[44] also suggests a linear relationship between the plastic shear strain and dimension of the mesh. Considering the hypothetical nature of the study, it was not possible to recalibrate the model parameters to extensometer measurements of Walton et al.[9] Instead, a linear scaling factor of 1.9 (mesh size in Walton et al.[9] was 0.3125 m in comparison to 0.166 m in this study) was chosen to approximately account for the grid dependency.

Dilation angle plays a major role in the damage evolution process within a pillar. With the onset of yield, inelastic lateral strains develop which typically increases the confinement in the system. This is a localized phenomenon but has global implications on pillar behavior. The minimum principal inelastic strain is mathematically related to the maximum principal inelastic strain through the dilation angle.[45] Several studies have found that the dilation angle is a function of the confining stress and the plastic shear strain and can be represented by a mathematical model.[45–48] Accounting for this mobilized nature of dilation angle is necessary to completely capture the micro-damage processes within a pillar. For that purpose, the Walton-Diederichs (WD) dilation angle model has been employed in this study.[45] It must be noted here that the particular dilation model used in this study is not too critical; the authors expect other mobilized dilation models to yield similar results. The relevant parameters for the pillar model were taken from Walton et al.[9] to reasonable capture the brittle dilation of Creighton granite. The parameters represent a pre-peak dilation with a faster decay in the post-peak portion, consistent with brittle rock behavior. The reader is referred to Walton and Diederichs[45] for details on selection of WD input parameters.

FLAC$^{3D}$ provides the flexibility of customizing the data-extraction process through the use of built-in programming language called FISH. Three table functions were developed for this study which recorded the maximum principal stress, minimum principal stress and the cumulative plastic shear strain for every element in the pillar. Since this is a computationally intensive process, the three variables were recorded every 2000 solution steps. Another FISH function was defined to measure the average relative displacements of the top and bottom of the pillar. These relative displacements were later converted to strain by dividing by the pillar height.

A total of eight model geometries corresponding to width-to-height ($W/H$) ratios of 0.5, 1, 1.5, 2, 2.5, 3, 3.5 and 4 were set up. The width of all the models were kept constant at 8 m while the height was varied. To ensure homogeneity of the applied strain, the velocity was scaled with respect to pillar height and is represented by the following equation:

**Table 1**
Thresholds and rock mass parameters relevant to the Granite pillar model.

| Segments of the S-shaped envelope | Threshold in $\sigma_1$-$\sigma_3$ space | Model Input Parameters | | Plastic shear strain (milli) |
|---|---|---|---|---|
| | | Cohesion (MPa) | Friction (degrees) | |
| Yield (Left portion) | $\sigma_1$-$\sigma_3$ = 81 | 40.5 | 0 | 0 |
| Yield (Right portion) | $\sigma_1$-3.8$\sigma_3$ = -31.2 | − 8.0 | 35.7 | |
| Intermediate (Left portion) | $\sigma_1$-2.2$\sigma_3$ = 15.6 | 5.3 | 22 | 5 |
| Intermediate (Right portion) | $\sigma_1$ = 2.6$\sigma_3$ | 0 | 25.9 | |
| Peak (Left portion) | $\sigma_1$-5.6$\sigma_3$ = 24.7 | 5.3 | 44.0 | 10 |
| Peak (Right portion) | $\sigma_1$-2.7$\sigma_3$ = 140.8 | 43.2 | 26.9 | |
| Residual (Left potion) | $\sigma_1$-3.9$\sigma_3$ = 0.4 | 0.1 | 36.3 | 50 |
| Residual (Right portion) | $\sigma_1$-3.5$\sigma_3$ = 17.5 | 4.7 | 33.6 | |

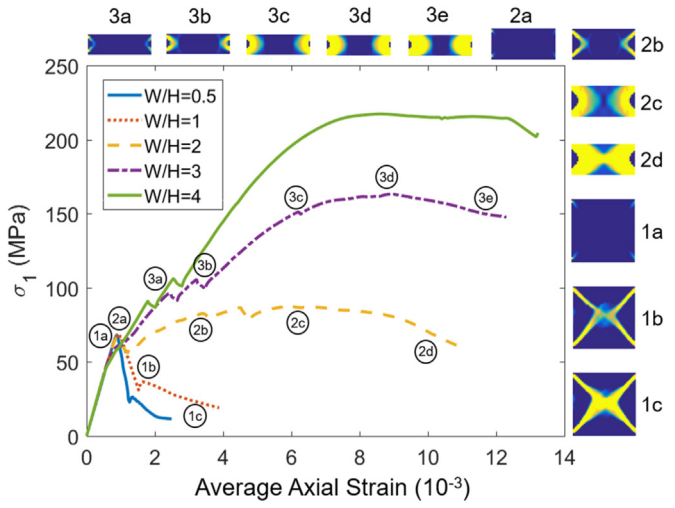


**Fig. 4.** Average stress-strain curve for $W/H$ of 0.5, 1, 2, 3 and 4 with shear band formation along the edges of the figure.

$$V\,(m/step) = 5x10^{-8}\frac{Height}{8} \tag{5}$$

All eight models were allowed to equilibrate until the global strengths were captured. Since the applied velocities were lower for squatter pillars and the failure transitioned from a brittle to ductile mechanism, more solution steps were required for larger $W/H$ pillar models. The model was evaluated by comparison of outputs with empirical pillar strength curves, the hourglass shape of the pillar core[49] and the development of stresses along the mid-section of the pillar.[50] The authors believe that the robustness of the developed yield criterion could be fairly substantiated on the basis of these assessments.

### 3.2. Model results

Fig. 4 shows the stress-strain curves obtained for $W/H$ ratios of 0.5, 1, 2, 3 and 4. In the models, the failure behavior transitioned from a brittle to ductile mechanism with increase in the $W/H$ ratio. With increase in $W/H$ ratio, the proportion of the outer shell/confined core[51] increases causing the strength to escalate. The rate of increase in strength is expected to decline with higher $W/H$ ratio, which most of the previous continuum numerical models[12–15] failed to capture. An exponential increase in strength beyond $W/H$ of 1.5–2.0 as observed from previous continuum modelling attempts would imply that such pillars are practically indestructible.

The $W/H$ ratio of 2 defines the transition from a brittle to ductile behavior. This is strictly dependent on the rock type under study and is a result of the complex interaction of the constitutive model, geomechanical parameters and dilation angle. There is a drastic increase in strength between $W/H$ of 2 and 3. To perceive the underlying reason, the elemental stress states for $W/H$ of 2 and 3 were plotted at their peak strength (Fig. 5). It was found that the strength of $W/H = 2$ pillar is majorly controlled by a combination of the spalling limit (left side of the peak envelope) and the CI threshold (left portion of the yield envelope) while for $W/H = 3$, it is mainly the spalling limit and the modified Mogi's line. A greater proportion of the stress states (% in Fig. 5) exceeded $\sigma_3 = 40.5$ MPa line for $W/H = 3$. Since the squatter pillar strengths were being controlled by the right side of the yield and peak envelope, a drastic jump is natural.

There is some amount of non-linearity in the stress-strain curve prior to achieving the peak strength. This hardening is more discernible for higher $W/H$ ratios as it occurred over a wider range of axial strain. In slender pillars, there is geometric freedom for formation of cross shear planes, causing a near-immediate collapse. This is illustrated through plastic shear strain plots (Fig. 4) for different loading stages. The localization of plastic yield initiates at the corner followed by the formation of a through-going concave shear plane. The geometric constraint in squatter pillars prevents the formation of such through-going shear planes, restricting damage to the outer portions of the pillar. Since the evolution of the stress-strain curve is guided by the increasing yield in the system, squatter pillars showed enhanced hardening behavior.

Interestingly, pillars with $W/H > 1$ continued to carry load over significant ranges of strain after achieving their peak strengths. This is significant from the perspective of pillar design, since most pillar design methodologies only consider the peak strength of pillars. For example, although pillars with $W/H = 1$ and $W/H = 2$ have nearly identical peak strengths, $W/H = 2$ may be sufficient to ensure stability due to their continued load carrying capacity following the attainment of peak strength. Fig. 6 shows the total plastic energy/m$^3$ dissipated at the first major drop in the stress-strain curve. If the energy dissipation process of a pillar system can be controlled through use of appropriate support, then the overall pillar dimension can be properly optimized through an understanding of its energy dissipation capacity.

The average stress-strain curve only provides a broad overview of the failure behavior of pillars. A complete understanding requires interpretation of both the micromechanical damage mechanisms and their emergent effect on the macroscopic behavior. To that end, the stress and plastic strain path of a central element (point iii, Fig. 7a) for the $W/H = 3$ model has been plotted (Fig. 7b and c). Initially, with increase in applied strain, the stress in this sampled zone follows the yield envelope up to 57 MPa confinement without undergoing any yield (eps ~0). The increase in confinement and axial stress in this portion of the curve is related to the dilation of peripheral elements. Since damage propagates inward, an element located on the outer side of the sampled element will be slightly more damaged at any particular point in time. This is displayed in Fig. 7c where the plastic strain paths for the sampled element and an adjacent element are represented by solid and dotted line, respectively.

In an attempt to explain the series of complex interactions that occurred within the models, 8 points on the two plastic strain curves were chosen (N', S', N'', S'' etc. in Fig. 7c). With onset of inelastic deformation, the neighboring element experienced more dilation than the sampled element (S', N'). The confining stress, as a result, reduced in the neighboring element but increased in the sampled zone. Beyond S', sufficient damage nucleated in the sampled zone allowing it to dilate and subsequently raise the confinement in the neighboring element (note the confinement change from N' to N'' and S' to S''). Such a loading-unloading process is typical and was noted in all the pillar models.

Both the elements continued to dilate and relax between N'', S'' and N''', S''' leading to a further reduction in the load carrying capacity of the sampled zone. Note the lower confinement and higher plastic strain localization at N''' in comparison to S'''. Late in the pillar damage process, at N'''' and S'''', the sampled and the neighboring element possess the same level of plastic damage.

The initial behavior of each element is localized and is majorly controlled by its immediate adjacent neighbors. However, with sufficient damage, the behavior transitions from a local to a global scale whereby a group of zones govern the deformation and stress pattern. For clarity of understanding, four points (namely i, ii and iv, in addition to Point iii; see Fig. 7a) were selected. Their locations were chosen to ensure that the local behavior of the inner and outer portions of the pillar could be adequately captured. This was necessary to understand how small scale damage processes lead to a macroscopic pillar failure.

The evolution of confinement for the four points was plotted against the solution step number (Fig. 7d). Some interesting observations and conclusions can be derived from this figure: (a) The step number corresponding to the first drop in confining stress is higher for points located deeper into the pillar. This is consistent with the fact that damage progresses from the outer to inner regions. (b) The segment bounded by

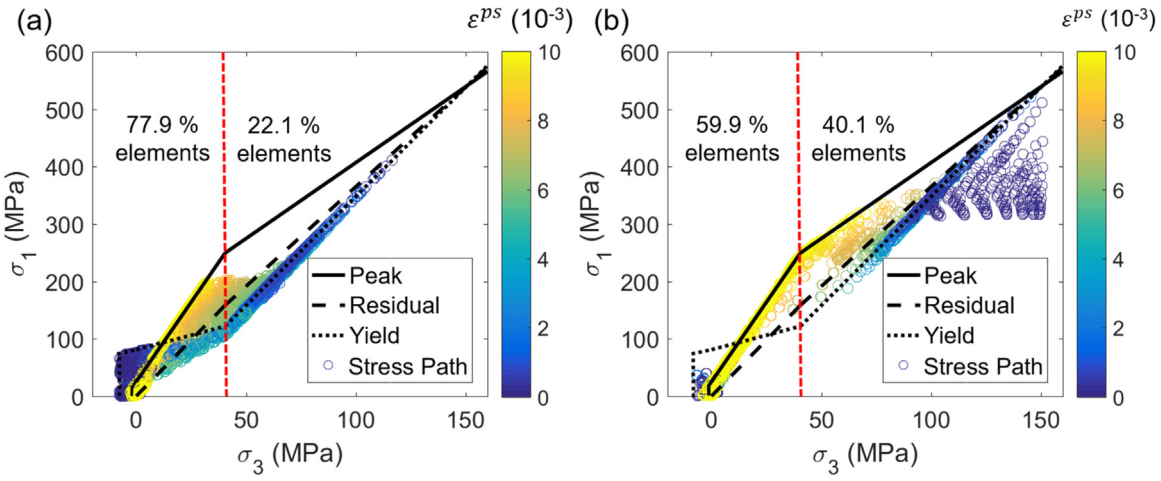


**Fig. 5.** Elemental stress states colored by plastic shear strain for (a) $W/H = 2$, (b) $W/H = 3$. (For interpretation of the references to color in this figure legend, the reader is referred to the web version of this article.)

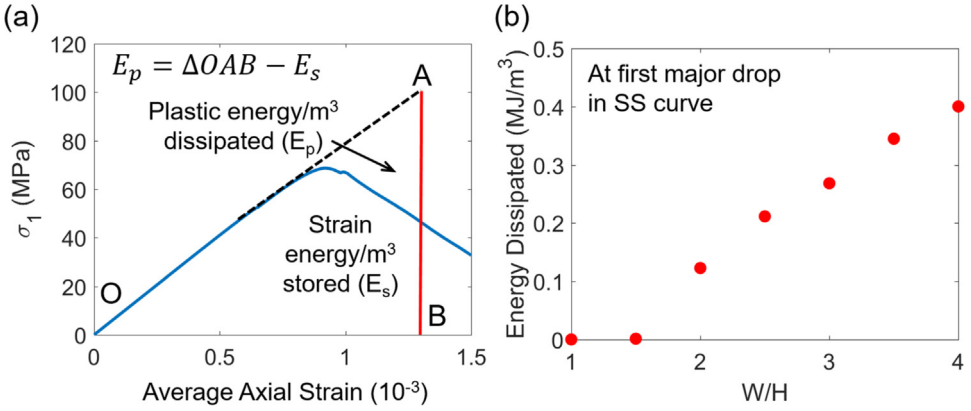


**Fig. 6.** (a) Calculation of dissipated plastic energy per unit volume from stress-strain curve, (b) Total plastic energy per unit volume dissipated for different $W/H$ models.

green lines shows that the confinement reduces for Points i and ii but increases for iii and iv. Physically, the outer portions are dilating, resulting in a confinement increase in the pillar core. It is very clear that instead of local interactions, the behavior of the pillar elements is actually being governed by blocks/slabs whose thickness vary with progressive loading. (c) The section bounded by black lines also demonstrates an increase in confinement for points iii and iv and some relaxation for i and ii. The fall in the confinement stress path for point iii coincides with the axial stress reversal in Fig. 7b and the reversal in Fig. 7c (see between N''', S''' and N'''', S''''). (d) The simultaneous rise in confinement for point ii, point iii & iv in the narrow region between the green and black demarcated zones in Fig. 7d occurs due to dilation of the first 1–1.5 m of the pillar edge (refer to the continued fall in confinement of point i in this region).

A logical concern is that the stress path may follow the residual envelope producing pillars with infinite strength. Such a behavior has indeed been demonstrated in previous modelling studies.[12,14,15] In this case, where the S-shaped criterion is used in conjunction with WD dilation model, the inverse relationship of dilation angle with plastic strain and confinement creates a feedback loop limiting the magnitude of confinement that could be generated in the core. Thus, with continued loading, the core yields followed by a complete collapse. It is very important to realize here that the selection of a dilation model is equally important as is the selection of a yield criterion. Failure to account for both these aspects could lead to unrealistic results being obtained.

A pillar subjected to increasing load (e.g. during sequential excavation of stopes) exhibits six failure stages as defined by Krauland and Soder[49]: (a) No fractures, (b) Slight spalling of pillar corners and pillar walls, (c) One or few fractures near surface with distinct spalling, (d) Fracturing in central parts of the pillars, (e) One or a few fractures occurring through central parts of the pillar, dividing it into two or several parts, and, (f) Disintegration of the pillar forming a well-developed hour-glass shape with central part completely crushed. The six stages of failure were suggested by Krauland and Soder[49] on the basis of field observations. A reliable pillar model should be able to capture most of these stages. An attempt is made here to perform a direct comparison to establish the credibility of the developed yield criterion. Specifically, two aspects of a failing pillar are targeted: (a) hourglass shape of the core, and, (b) progressive localization of stress along the mid height of the pillar.

Fig. 8(a, b) shows the stress concentration around the core of the pillar for W/H of 2 and 3. As a pillar is perpetually loaded, the sides spall off which channels the excess load though the core - the shape of this highly stressed volume is similar to an hourglass. The models developed in this study distinctly capture the hourglass shape for pillars with $W/H > 1$. In slender pillars, the formation of through-going shear planes prevent the development of any confined core. The larger base of the hourglass for wider pillars reflects their higher load-carrying capacity.

Fig. 8(a, b) only illustrates the stresses corresponding to the solution step when the global peak strengths were achieved. It, however, does not show the evolution of these stresses as the model is subjected to increasing load. To that end, six stages were selected for $W/H = 3$

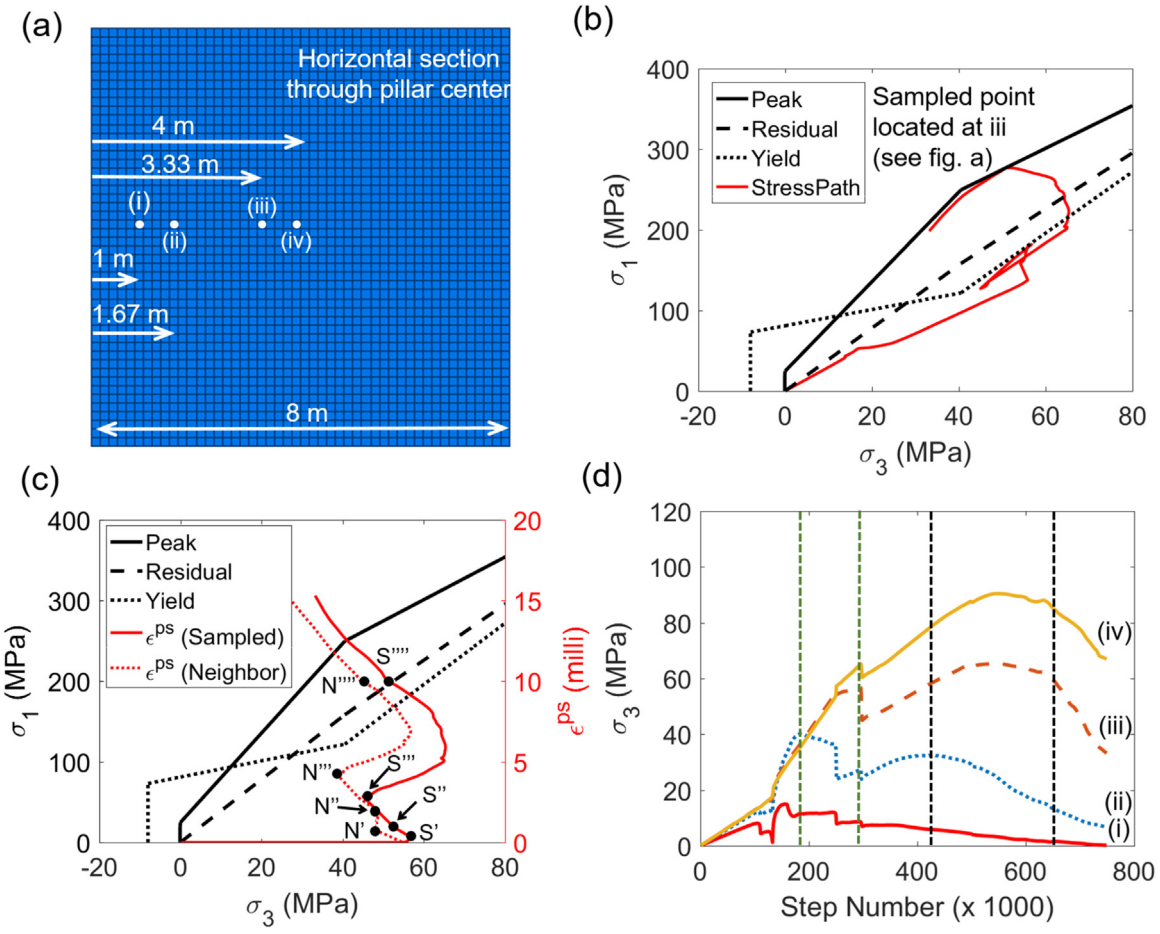


**Fig. 7.** (a) Location of the four points on a horizontal section along the center of the $W/H = 3$ pillar, (b) Stress-path for an element located at the center of $W/H = 3$ pillar, (c) Plastic-shear strain path for the sampled point and an adjacent element, (d) Confinement path of Points i, ii, iii and iv as a function of step number.

model that could adequately bracket the temporal variation of stresses within the pillar (Fig. 8c-h). The plots provided show maximum principal stress ($\sigma_1$) along a horizontal plane passing through the pillar center. The results are similar to the boundary-relaxation-core-loading phenomenon observed by Wagner[50] in field. As spalling initiates, the peripheral elements start to yield, pushing the stresses deeper into the pillar. The excellent correspondence with the findings of Wagner[50] is intuitively satisfying and serves to further support the robustness of the progressive S-shaped criterion.

## 4. Comparison to empirical pillar strength database

### 4.1. Pillar database and progressive S-shaped criterion results

Over the years, there has been significant development in rock mass characterization techniques and numerical modelling capabilities. Despite these advances, pillar design continues to rely predominantly on empirical formulae and design charts. Both these approaches are based on statistical analysis of field observations with empirical/numerical estimation of stresses. A variety of methods ranging from tributary area theory[16] to more complex two/three dimensional finite element[52] and boundary element modelling[49,53] were utilized in past for estimating the average pillar stresses at the point of failure.

Most of the numerical modelling works considered the rockmass to be homogenous, isotropic and perfectly elastic. Although this may be an acceptable approximation in some cases, it does not account for the loss in load carrying capacity due to plastic yield and subsequent loading of the neighboring pillars. It also does not consider the fact that some of the failures may be structure-driven rather than stress-driven, particularly for lower $W/H$ pillars. In the room and pillar mining method, where the pillars are equidimensional and located in a near-regular grid, there could be multiple pillars subjected to elevated stress level rendering the selection of one failed pillar practically impossible. Despite the limitations inherent in any individual study, the empirical systems overall work well and represent a reliable starting point for design.

Most empirical formulae and charts relate the normalized strength to the W/H ratio of pillars. In context of rock pillars, the well-known works are those of Lunder and Pakalnis,[17] Krauland and Soder,[49] Potvin et al.[53] Sjoberg[54] and Hudyma[55] with Hedley and Grant's[16] being the most commonly used pillar design formula. Despite its popularity, its formulation has been based on some radical assumptions that may or may not be applicable to all geo-mining conditions.[56] Firstly, the power-law form of the equation, adopted from the Salamon and Munro[57] formula, was developed for square pillars; the Uranium mine database that Hedley and Grant used comprised of long slender pillars. The inherent assumption then is that the strength of square pillars is more or less similar to long slender pillars. Secondly, the entire formulation was constrained by only three failed pillar cases in contrast to 27 failed cases in Salamon and Munro.[57] Thirdly, the simplistic tributary area concept, combined with horizontal stress estimates from two nearby mines, was used to compute the failure load of the inclined pillars. The question then remains is how has it been successfully implemented in pillar design all over the world? One possible reason could be that although the formulating database considered hard rocks ($UCS = 210$ MPa), its successful application may have been restricted to moderate strength ($UCS < 200$ MPa) rock pillars only.

A major concern in some of the listed studies is the fact that a

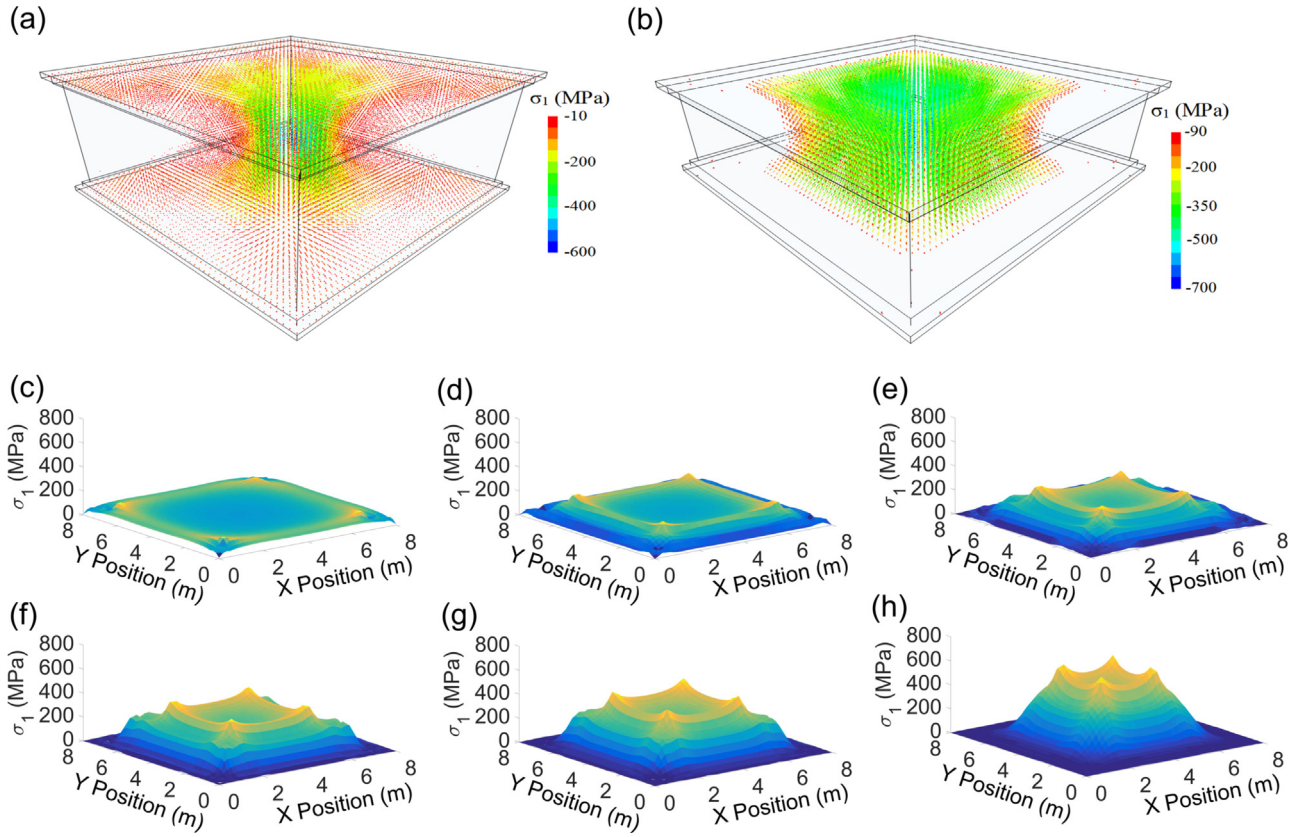


**Fig. 8.** Concentration of vertical stress around the core of the pillar with (a) $W/H = 2$, (b) $W/H = 3$; (c-h) development of vertical stress along the mid-height of the pillar with increasing damage.

variety of rocks with different mechanical characteristics were considered before segregating the datasets.[17,53] Even though the pillar strengths were normalized to *UCS* to account for the variability in geology, other factors (like brittleness, dilation etc.), which affect the *W/H* trend in strength, were neglected. In the absence of additional information on rock properties, UCS was chosen as a proxy for those other factors in this study. First, all available datapoints in literature were combined and then filtered into three cases: a) Soft: *UCS* in the range 70–140 MPa, b) Moderate: *UCS* in the range 140–200 MPa, and c) Hard: *UCS* in the range 200–300 MPa. Fig. 9(a-c) shows the three groups with a visually estimated line separating stable and failed case histories.

With increase in *UCS*, a rightward shift in the steep portion of the curve was noticed (Fig. 9d). If the segregation was not performed and the entire dataset was used instead, then all three divisions would be expected to follow a single trend. The difference in the shape is not a mere coincidence; it is related to the brittleness and dilation characteristics of the rock type. The friction angle of the CI threshold has been found to decrease with increase in rock *UCS*.[39] Stronger rocks typically exhibit a larger lag between the mobilization of friction and degradation of cohesion. The delay in strength mobilization prevents pillar-scale hardening behavior from occurring at moderate *W/H* ratios. Additionally, in context of dilatancy, stronger rocks tend to maintain their capacity to dilate under confined conditions more in the early stages of inelastic deformation[45] which means that smaller pillar cores in moderate *W/H* ratio pillars can dilate and lose confinement more readily.

Fig. 10a shows the model results obtained using parameters representative of Creighton Granite compared with the failed, unstable and stable case histories for the *UCS* group 200–300 MPa. The progressive S-shaped criterion model clearly delineates between the stable and failed case histories, and the overall convex shape is consistent with what has been historically associated with this type of relationship.[16,17] Up to a *W/H* of 1.5, the strength is practically constant while it increases drastically between *W/H* of 1.5 and 2.5. The increase in strength with W/H has been demonstrated extensively in the past; the shape, however, does not conform with Martin and Maybee[12] Mortazavi et al.[14] and Kaiser et al.[15] Due to unavailability of failed/unstable datapoints, the squatter portion of the curve could not be well constrained; the trend, nonetheless, is consistent with the expected convex shape.

For purposes of comparison, the model outputs have been overlaid with different pillar strength equations and the three previous modelling results (Fig. 10b). Except for Krauland and Soder[49] all the other equations seem to over-predict the strength of slender pillars. This is not unlikely given that Lunder and Pakalnis[17] did not segregate the dataset while Krauland and Soder[49] and Von Kimmelman et al.[52] developed the empirical curves for rocks with *UCS* of 94 MPa (sulphide ore in Limestone) and 100 MPa (metasediments), respectively. The issues related to the study by Hedley and Grant[16] have been discussed previously. It becomes apparent that segregation of the dataset and understanding the domain of applicability of the empirical design methods are a necessity to correctly estimate pillar strengths in a particular geological setting. Another interesting observation is that both Krauland and Soder[49] and Lunder and Pakalnis[17] underestimate the strength of squatter pillars. The development of these empirical methods required classifying pillars under stable, failed and unstable groups through visual examination. Oftentimes, squatter pillars exceed their serviceability limits through surficial spalling processes but their core remains intact. Hence, a pillar which may have been classified as 'failed' may actually be capable of carrying additional load. Misinterpretation of pillar states in the formulating database could be a probable reason for the observed strength discrepancy. In context of the numerical modelling results, the stark difference in trend is likely related to the inability of the three criteria

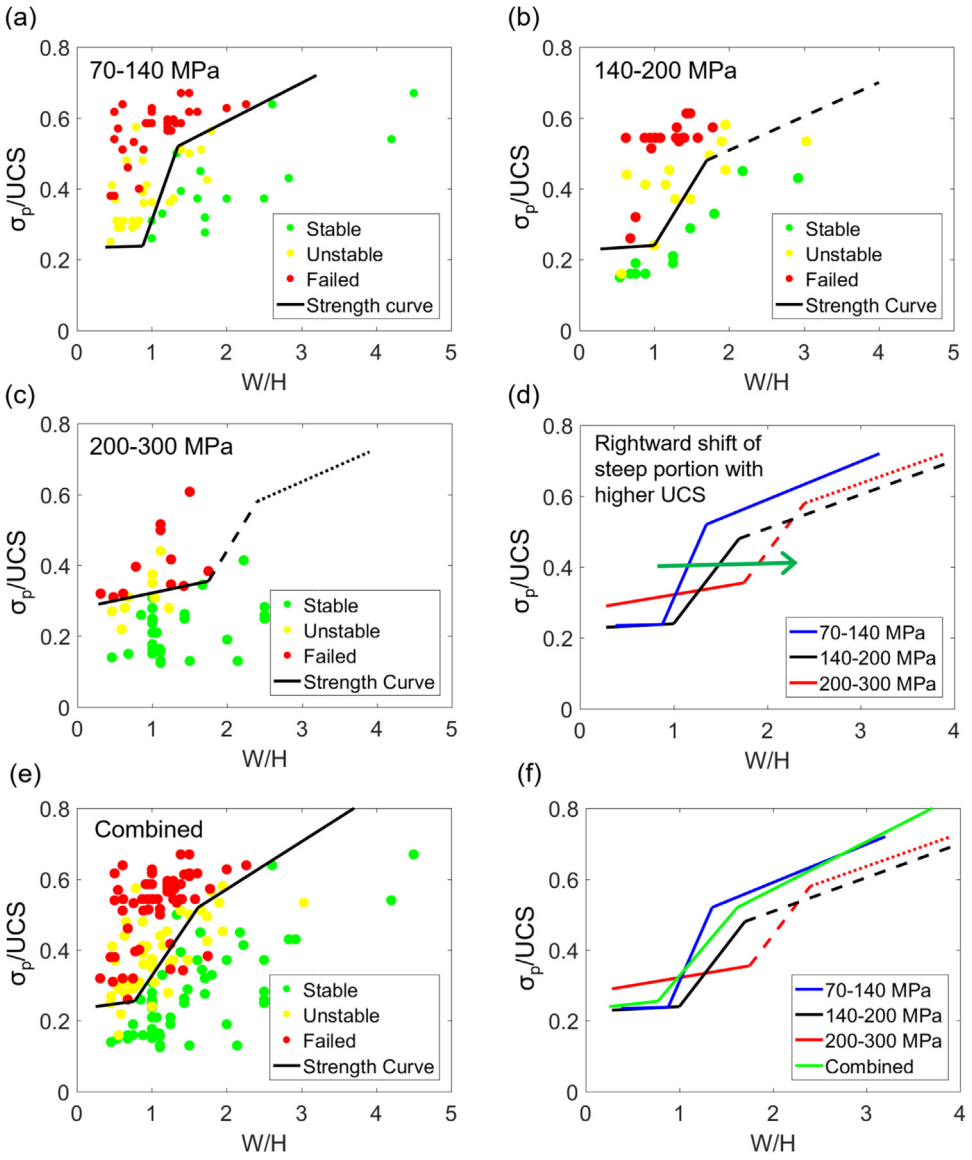


**Fig. 9.** Empirical strength database divided into (a) *UCS*: 70–140 MPa, (b) *UCS*:140–200 MPa, (c) *UCS*: 200–300 MPa; (d) comparison of the strength envelopes for each *UCS* range; (e) Combined database; (f) comparison of the three division with the combined database.

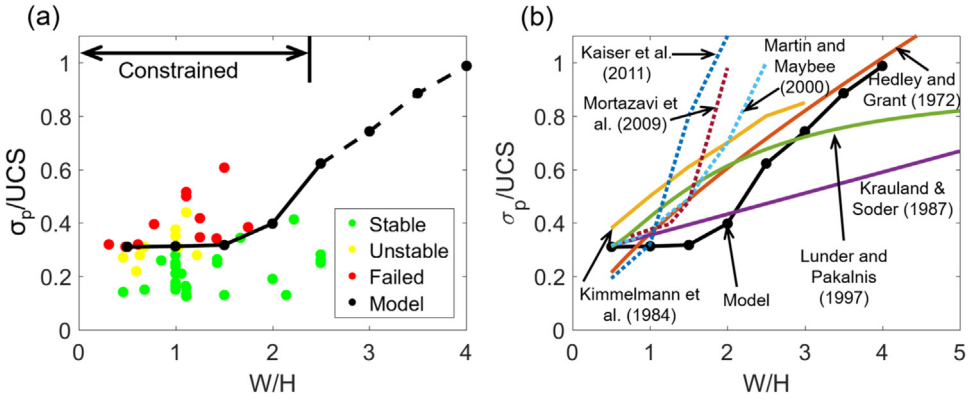


**Fig. 10.** (a) Stable, unstable and failed cases (*UCS* > 200 MPa) with black line indicating model results, (b) Comparison of progressive S-shaped results with empirical strength equations and previous modelling attempts.

**Table 2**
Thresholds and rock mass parameters relevant to the Conglomerate pillar model.

| Segments of the S-shaped envelope | Threshold in $\sigma_1$-$\sigma_3$ space | Model Input Parameters | | Plastic shear strain (milli) |
|---|---|---|---|---|
| | | Cohesion (MPa) | Friction (degrees) | |
| Yield (Left portion) | $\sigma_1$-1.8$\sigma_3$ = 42.5 | 16 | 16 | 0 |
| Yield (Right portion) | $\sigma_1$-3.2$\sigma_3$ = 31.5 | 8.8 | 31.6 | |
| Peak (Left portion) | $\sigma_1$-12.2$\sigma_3$ = 5.6 | 0.8 | 58 | 6.8 |
| Peak (Right portion) | $\sigma_1$-2.4$\sigma_3$ = 80 | 26 | 24 | |
| Residual (Left potion) | $\sigma_1$-3.8$\sigma_3$ = 2.9 | 0.8 | 36 | 34 |
| Residual (Right portion) | $\sigma_1$-3.7$\sigma_3$ = 4.2 | 1.2 | 34.8 | |

to capture the damage mechanisms of intact rocks, augmented by an inaccurate representation of dilation angle. A detailed comparison of the four criteria is a topic for future research.

### 4.2. Model behavior for weaker rock

The grouping of the empirical database reveals the mechanistic differences in pillar failure mechanisms as a function of its constituent material. Indeed, the behavior of a softer pillar is different from a harder one – a fact that many previous studies have neglected. Fig. 9(e-f) compares the strength curves obtained from the three groups to that fitted to the entire database. Clearly, *W/H* ratio corresponding to the steep increase in strength is overestimated for stronger rocks (*UCS* > 140 MPa). For a *W/H* ratio of 1–2, the combined curve predicts a much higher strength than the 200–300 group. The 200–300 MPa group represents brittle rocks where the extent of spalling controls the peak strength.

To demonstrate the ability of the progressive S-shaped criterion to capture the varying trends in the strength curve, a weaker rock type (a conglomerate with a *UCS* of 95 MPa) was modeled based on the parameters provided by Walton and Diederichs.[10] To make a more focused comparison with the empirical database, only pillar case studies with *UCS* values between 75 MPa and 125 MPa were considered. Because the original study in Walton and Diederichs[10] used the CWFS strength model, some of the outstanding parameters of the progressive S-shaped criterion had to be estimated on the basis of engineering judgement. The parameters were then adjusted to calibrate the model strength results to the empirical data. The same model geometry and loading conditions, as described in Section 3.1, were used. A total of 7 models were simulated with *W/H* of 0.5, 1, 1.5, 2, 2.5, 3 and 3.5.

Table 2 lists the rockmass parameters for the Conglomerate model; the post-yield dilation parameters were chosen from Walton and Diederichs[10] to represent a moderate strength rock with slower dilation decay in the post-peak portion of the model. Unlike Creighton granite, the mobilization of friction and degradation of cohesion occurs for the same value of plastic shear strain. This is one of the main reasons, in addition to dilation angle model changes, for the disparity seen in the trend of the strength curves. The average stress-strain curves for *W/H* = 1, 1.5, 2, 3 and the model peak strengths overlaid with the empirical database are shown in Fig. 11(a, b). The model results were able to replicate the increase in pillar strength between the *W/H* = 0.5 and *W/H* = 1.5 cases as shown in the empirical data. The ability of the model results to separate the failed and stable case histories within the constrained domain for both stronger more brittle rock types (i.e. Creighton granite) and rocks with a more moderate strength (i.e. conglomerate) suggests that the progressive S-shaped criterion has broad applicability.

## 5. Conclusion

This study has presented an improved rock yield criterion that has the capability of capturing small-scale damage processes while exhibiting an emergent pillar behavior consistent with what has been observed in the field. It accounts for extensile-spalling behavior in low confinement areas and shear based failure in high confinement areas using plastic shear strain as a proxy to damage. Most of the defining parameters are related to damage threshold levels and can be obtained through laboratory rock testing. In absence of such testing, the reader can refer to the guidelines proposed by Walton[39] as a starting point followed by calibration of the most uncertain parameters to achieve a better fit to field measurements.

Numerical models of pillar loading successfully demonstrated the hourglassing of the pillar core and the progressive localization of stress along the mid-section in agreement with the findings of Krauland and Soder[49] and Wagner.[50] Some of the previous empirical studies on pillar strength considered a variety of rocks with significantly different *UCS*. Such a classification may not be accurate in explaining the behavior of pillars within a particular rock type. As a solution, this study has

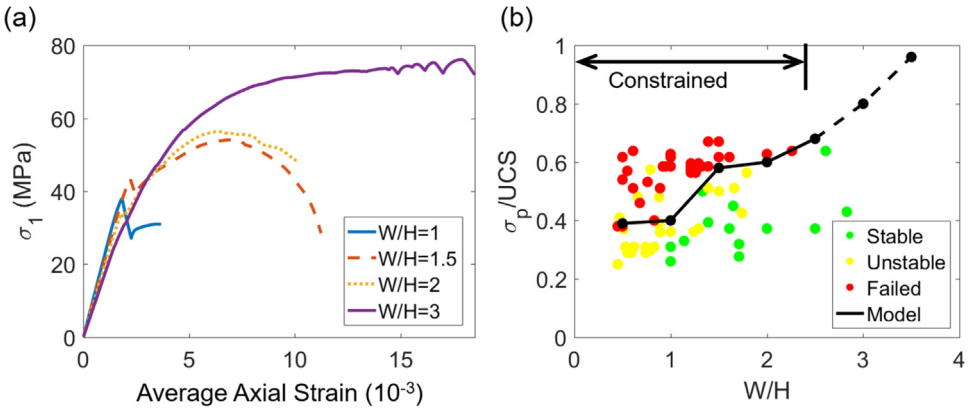


**Fig. 11.** (a) Average stress-strain curve for Conglomerate pillar models, (b) Stable, unstable and failed cases (75 < *UCS* < 125 MPa) with black line indicating model results.

segregated the database by *UCS* and utilized two end-member groups to assess the validity of the numerical models. It was found that the progressive S-shaped criterion can successfully encompass the failure mechanisms in rock pillars composed of both very strong and moderate strength rocks.

The rock pillar model developed in this study was subsequently utilized in assessing the effect of W/H ratio on the pillar strength. The models predicted an overall convex trend which is consistent with empirical findings but in contradiction with previous modelling studies. The choice of yield criterion and representation of the dilation angle seemed to be the root cause for this disparity. Nonetheless, the criterion developed in this study was successful in representing the behavior of rock pillars. Further endeavors are being made to generalize the selection of the input parameters for different rock types.

## Acknowledgement

The research conducted for this study was funded by the National Institute of Occupational Health and Science (NIOSH) under Grant Number 200-2016-90154. The authors would like to extend their sincere gratitude for this financial support.

## References

1. Fairhurst C, Pei J. A comparison between the distinct element method and the finite element method for analysis of the stability of an excavation in jointed rock. *Tunn Undergr Space Technol.* 1990;5(1–2):111–117.
2. Hajiabdolmajid V, Kaiser PK, Martin CD. Modelling brittle failure of rock. *Int J Rock Mech Min Sci.* 2002;39 [731-341].
3. Shan XY, Mei HB, Xu DQ, Zhao YX. Mining-induced influences on stability of floor haulage roadway in tectonic stress field. *Yanshilixue Yu Gongcheng Xuebao/Chin/J Rock Mech Eng.* 2005;24(12):2101–2106.
4. Edelbro C. Numerical modelling of observed fallouts in hard rock masses using an instantaneous cohesion-softening friction-hardening model. *Tunn Undergr Space Technol.* 2009;24:398–409.
5. Zhao XG, Cai M, Cai M. Considerations of rock dilation on modeling failure and deformation of hard rocks—a case study of the mine-by test tunnel in Canada. *J Rock Mech Geotech Eng.* 2010;2:338–349.
6. Kang Y, Liu Q, Gong G, Wang H. Application of a combined support system to the weak floor reinforcement in deep underground coal mine. *Int J Rock Mech Min Sci.* 2005;71:143–150.
7. Sinha S, Chugh YP. An evaluation of roof support plans at two coal mines in Illinois using numerical models. *Int J Rock Mech Min Sci.* 2015;82:1–9.
8. Chugh YP, Sinha S. Numerical modeling of roof support plans at 4-way coal mine intersections. In: *Proceedings of the 49th US Rock Mechanics Symposium*, San Francisco; June 2015.
9. Walton G, Diederichs MS, Punkkinen A. The influence of constitutive model selection on predicted stresses and yield in deep mine pillars-A case study at the Creighton mine, Sudbury, Canada. *Geomech Tunn.* 2015;5:441–449.
10. Walton G, Diederichs MS. A mine shaft case study on the accurate prediction of yield and displacements in stressed ground using lab-derived material properties. *Tunn Undergr Space Technol.* 2015;49:98–113. http://dx.doi.org/10.1016/j.tust.2015.04.010.
11. Sinha S, Chugh YP. Modified roof control plans for intersections in an Illinois coal mine. In: *Proceedings of the 50th US Rock Mechanics Symposium*. Houston; 26–29 June 2016.
12. Martin CD, Maybee WG. The strength of hard rock pillar. *Int J Rock Mech Min Sci.* 2000;37:1239–1246.
13. Iannacchione AT. Analysis of pillar design practices and techniques for US limestone mines. *Trans Inst Min Metall (Sect A: Min Ind).* 1999;108:A152–A160.
14. Mortazavi A, Hassani FP, Shabani M. A numerical investigation of rock pillar failure mechanism in underground openings. *Comput Geotech.* 2009;36–5:619–697.
15. Kaiser PK, Kim B, Bewich RP, Valley B. Rock mass strength at depth and implication for pillar design. *Min Technol.* 2011;120(3):170–179.
16. Hedley DGF, Grant F. Stope, pillar design for the Elliot Lake uranium mines. *Can Inst Min Metall Bull.* 1972;65:1165–1186.
17. Lunder PJ, Pakalnis R. Determining the strength of hard rock mine pillars. *Bull Can Inst Min Metall.* 1997;90:51–55.
18. Martin CD. The effect of cohesion loss and stress path on brittle rock strength. *Can Geotech J.* 1997;34:698–725.
19. Read RS. 20 years of excavation response studied at AECL's underground research laboratory. *Int J Rock Mech Min Sci.* 2004;41:1251–1275.
20. Hoek E, Kaiser PK, Bawden WF. *Support of Underground Excavation in Hard Rock.* Rotterdam: Balkema; 1995:215.
21. Diederichs MS. Rock fracture and collapse under low confinement conditions. *Rock Mech Rock Eng.* 2003;36:339–381.
22. Diederichs MS, Kaiser PK, Eberhardt E. Damage initiation and propagation in hard rock during tunnelling and the influence of near-face stress rotation. *Int J Rock Mech Min Sci.* 2004;41:785–812.
23. Diederichs MS. Mechanistic interpretation and practical application of damage and spalling prediction criteria for deep tunnelling. *Can Geotech J.* 2007;44:1082–1116.
24. Martin CD, Chandler NA. The progressive fracture of Lac Du Bonnet granite. *Int J Rock Mech Min Sci.* 1994;31:643–659.
25. Martin CD, Kaiser PK, McCreath DR. Hoek-Brown parameters for predicting the depth of brittle failure around tunnel. *Can Geotech J.* 1999;36:136–151.
26. Pelli F, Kaiser PK, Morgenstrern NR. An interpretation of ground movements recorded during construction of the Donkin-Morien tunnel. *Can Geotech J.* 1991;28:239–254.
27. Kaiser PK, Kim B. Characterization of strength of intact brittle rock considering confinement-dependant failure processes. *Rock Mech Rock Eng.* 2015;48:107–119.
28. Paterson MS, Wong T. *Experimental Rock Deformation - the Brittle Field.* Netherlands: Springer; 2005.
29. Itasca. FLAC 3D Version 5.0: *Theory and Background.* Itasca Consulting Group, Minneapolis, Minnesota; 2016.
30. Walton G. *Improving continuum models for excavations in rock masses under high stress through an enhanced understanding of post-yield dilatancy [Ph.D. Thesis].* Kingston, Canada: Queen's University; 2014.
31. Ebarhardt E, Stead D, Stimpson B, Read R. Identifying crack initiation and propagation thresholds in brittle rocks. *Can Geotech J.* 1998;35(2):222–233.
32. Brace WF, Paulding B, Scholz C. Dilatancy in the fracture of crystalline rocks. *J Geophys Res.* 1996;71:3939–3953.
33. Lajtai EZ. Brittle fracture in compression. *Int J Fract Mech.* 1974;10:525–536.
34. Nicksiar M, Martin CD. Evaluation of methods for determining crack initiation in compression tests on low-porosity rocks. *Rock Mech Rock Eng.* 2012;45:607–617.
35. Walton G, Hedayat A, Kim E, Labrie D. Post-yield strength and dilatancy evolution across the brittle-ductile transition in Indiana Limestone. *Rock Mech Rock Eng.* 2017;50(7):1691–1710. http://dx.doi.org/10.1007/s00603-017-1195-1.
36. Mogi K. Pressure dependence of rock strength and transition from brittle fracture to ductile flow. *Bull Earthq Res Inst.* 1966;44:215–232.
37. Byerlee JD. Brittle-ductile transition in rocks. *J Geophys.* 1968;73(14):4741–4750. http://dx.doi.org/10.1029/JB073i014p04741.
38. Kaiser PK, Diederichs MS, Martin CD, Sharp J, Steiner W. Underground works in hard rock tunnelling and mining. In: *Proceedings ISRM International Symposium*. International Society for Rock Mechanics; 2000.
39. Walton G. Guidelines for the selection of input parameters for Cohesion-Weakening-Friction-Strengthening (CWFS) analysis of excavations in brittle rock. *Int J Rock Mech Geotech Eng.*; 2017. Submitted for publication.
40. Marinos P, Hoek E. GSI—a geologically friendly tool for rock mass strength estimation. In: *Proceedings GeoEng*, Melbourne, Australia; 2000: 1422–1442.
41. Hudson JA, Brown ET, Fairhurst C. Shape of the complete stress-strain curve for rock. In: *Proceedings of the 13th U.S. Symposium on Rock Mechanics*, Urbana (Edited by Cording E. J.); 1972: 773–795.
42. Diederichs MS, Martin CD. Measurement of spalling parameters from laboratory testing. In: Zhao Labiouse, DudtMathiereds. *Rock Mechanics in Civil and Environmental Engineering.* London: Taylor & Francis; 2010.
43. Ghazvinian E. *Modelling and Testing Strategies for Brittle Fracture Simulation in Crystalline Rock Samples [M.A.Sc. Thesis].* Kingston, Ontario: Queen's University; 2010.
44. Itasca. FLAC 3D Example Application Versionv6. Itasca Consulting Group, Minneapolis, Minnesota; 2016.
45. Walton G, Diederichs MS. A new model for the dilation of brittle rocks based on laboratory compression test data with separate treatment of dilatancy mobilization and decay. *Geotech Geol Eng.* 2015;33(3):661–679. http://dx.doi.org/10.1007/s10706-015-9849-9.
46. Alejano LR, Alonso A. Consideration of dilatancy angle in rock and rock masses. *Int J Rock Mech Min Sci.* 2005;42:481–507.
47. Zhao XG, Cai M. A mobilized dilation angle model for rocks. *Int J Rock Mech Min Sci.* 2010;47:368–384.
48. Walton G, Diederichs MS. Dilation and post-peak behavior inputs for practical engineering analysis. *Geotech Geol Eng.* 2015;33(1):15–34. http://dx.doi.org/10.1007/s10706- 014-9816-x.
49. Krauland N, Soder PE. Determining pillar strength from pillar failure observation. *Eng Min J.* 1987;8:34–40.
50. Wagner H. Determination of the complete load-deformation characteristics of coal pillars. In: *Proceedings 3rd Congress*, ISRM, Denver; 1974: 1067–1081.
51. Valley B, Kim B, Suorineni FT, Bahrani N, Bewick RP. Influence of confinement dependent failure processes on rock mass strength at depth. *Harmonising Rock Engineering and the Environment* – Qian & Zhou (eds), London, ISBN 978-0-415-80444-8; 2012.
52. Von Kimmelman MR, Hyde B, Madgwick RJ. The use of computer applications at BCL Limited in planning pillar extraction and the design of mining layouts. In: *Design and performance of underground excavations*. International Society of Rock Mechanics Symposium; 1984: 53–63.
53. Potvin Y, Hudyma M, Miller HDS. Rib pillar design in open stoping. *Can Inst Min Metall Bull.* 1989;82:31–36.
54. Sjoberg J. Failure modes and pillar behavior in the Zinkgruvan mine. In: *Proceedings of the 33rd U.S. Rock Mech Symposium*; 1992: 491–500.
55. Hudyma MR. *Rib Pillar Design in Open Stope Mining [M.A.Sc. Thesis].* The University of British Columbia; 1988.
56. Malan DF, Napier JAL. The design of stable pillars in the Bushveld complex mines: a problem solved? *J S Afr Ins Min Met.* 2011.
57. Salamon MDG, Munro AH. A study of the strength of coal pillars. *J S Afr Inst Min Metall.* 1967;68:56–67.